https://doi.org/10.5194/egusphere-2026-5208
Preprint. Discussion started: 28 September 2026

Peroxyacetyl nitrate persists across boundary-layer regimes and varies with transport pathway at an elevated East Asian receptor

Jinsang Jung[1], Sumin Ok[1,2], JiYi Lee[2]

[1]Gas Metrology Group, Korea Research Institute of Standards and Science (KRISS), Daejeon 34113, Republic of Korea
[2]Department of Environmental Engineering, Ewha Womans University, Seoul 03760, Republic of Korea

Correspondence to: Jinsang Jung (jsjung@kriss.re.kr)

Abstract. Peroxyacetyl nitrate (PAN) is a thermally reversible reservoir of reactive nitrogen that redistributes ozone-production potential from NO_x source regions. Its persistence at elevated East Asian receptors under interacting transport, photochemistry, and boundary-layer exchange remains poorly constrained. We investigated PAN at the summit of Mount Gaya, Korea (678 m a.s.l.), during the same spring periods in 2022 and 2023 using paired photolytic- and molybdenum-converter NO_2 measurements, direct PAN observations, ERA5 boundary-layer diagnostics, and 72 h HYSPLIT backward trajectories. The converter difference, defined as operational gas-phase NO_z^* (= $NO_{2,Moly} - NO_{2,Photo}$), averaged 2.12 ppbv in both campaigns and represented 57.5–58.0 % of the molybdenum-converter response. In 2023, PAN averaged 0.64 ± 0.51 ppbv, and the ratio of campaign-mean PAN to campaign-mean NO_z^* was 30.2 %. PAN/NO_z^* ratios showed no systematic enhancement under boundary-layer-decoupled conditions after temporal autocorrelation was considered. Trajectory-level median PAN was 0.66 ppbv for Continental East Asia, 0.58 ppbv for Korean Peninsula regional, and 0.35 ppbv for Marine/Background pathways, with a significant overall pathway dependence. In contrast, median PAN/NO_z^* ratios of 33.2 %, 28.2 %, and 28.5 %, respectively, did not differ significantly among pathways. PAN-rich episodes further showed that the largest PAN enhancement and the highest PAN/NO_z^* ratio occurred under different transport conditions. These observations indicate that PAN persistence at Mount Gaya reflects the combined influence of continental transport, regional photochemical processing, and vertical exchange rather than boundary-layer isolation alone, and that PAN can constitute a substantial directly measured component of converter-responsive oxidized nitrogen.

1 Introduction

Nitrogen oxides (NO_x = NO + NO_2) are central to tropospheric ozone production, but their relatively short atmospheric lifetime limits direct transport far from emission regions. Peroxyacetyl nitrate (PAN; $CH_3C(O)O_2NO_2$) extends the spatial influence of NO_x by reversibly sequestering reactive nitrogen. PAN forms from the reaction of the peroxyacetyl radical with NO_2 and is thermally unstable in warm boundary-layer air, whereas it can persist for days to weeks under colder conditions aloft. Subsequent warming or downward transport promotes PAN decomposition and NO_2 release, thereby redistributing

https://doi.org/10.5194/egusphere-2026-5208
Preprint. Discussion started: 28 September 2026

reactive nitrogen and ozone-production potential to downwind regions (Fischer et al., 2014; Jiang et al., 2016; Flowerday and Hansen, 2026).

Global chemical transport modeling, aircraft campaigns, long-term mountaintop observations, and satellite retrievals have established PAN as an important reservoir and carrier of reactive nitrogen (Fischer et al., 2011, 2014; Zhai et al., 2024; Shogrin et al., 2024). Recent satellite observations have strengthened the direct observational evidence for this transport role. IASI observations have traced Asian PAN across the North Pacific, linking transported PAN to transpacific ozone pollution (Zhai et al., 2024), while a global CrIS analysis showed pronounced seasonal and interannual variability in PAN transport across Northern Hemisphere ocean basins, with April and July emerging as important months for transpacific transport (Shogrin et al., 2026). The latter study also found that transported PAN responded less strongly than NO_2 to large emission perturbations, illustrating the nonlinear relationship between precursor emissions and the PAN reservoir. New AIRS retrieval capabilities further extend the potential PAN satellite record and provide complementary information on free-tropospheric PAN distributions (Laughner et al., 2026). These satellite measurements, however, primarily constrain PAN aloft and provide limited information on its partitioning and vertical coupling in the lower troposphere over complex terrain.

In situ observations across East Asia further demonstrate that PAN reflects a combination of local photochemistry, precursor availability, temperature, and regional transport rather than a single controlling process (Lin et al., 2024; Liu et al., 2024; Hu et al., 2025). Multi-site observations in the Pearl River Delta showed a stronger role for regional transport in cold-season PAN at rural and coastal locations, whereas photochemical formation became more important during the warm season (Liu et al., 2024). High-resolution measurements and modeling in southeastern China have likewise demonstrated substantial summertime PAN formation under strong photochemical conditions and pronounced sensitivity to VOC precursors (Hu et al., 2025). Moreover, 5 years of measurements in urban Fuzhou showed a declining PAN trend despite increasing O_3, indicating that changes in PAN abundance and ozone pollution can diverge as precursor emissions and atmospheric conditions evolve (Lin et al., 2024). Together, these studies emphasize that PAN abundance cannot be inferred directly from NO_2 or O_3 alone and that its regional distribution depends on both chemistry and transport.

Recent aircraft measurements provide particularly relevant evidence for the Korean Peninsula. During the 2024 ASIA-AQ campaign, acyl peroxynitrates reached 5.5 ppbv over South Korea and the Yellow Sea, with median concentrations higher over the Yellow Sea and the mid- and southern Korean Peninsula than over the Seoul Metropolitan Area (Lee et al., 2026). These observations demonstrate that PAN-rich photochemically processed air is regionally extensive and can remain elevated away from the largest urban source region. However, aircraft campaigns provide temporally intensive but episodic snapshots. How PAN persists at continuously monitored elevated receptors in East Asia, and how that persistence depends on local vertical coupling versus preceding transport history, remain insufficiently constrained.

Mountaintop observations provide a complementary perspective because elevated sites can intermittently sample air above the local boundary layer while also experiencing direct boundary-layer influence. Such sites, however, cannot generally be regarded as continuously representative of the free troposphere, particularly over complex terrain. At Mount Gaya (678 m a.s.l.), ERA5-derived planetary boundary-layer height is typically below the summit during nighttime and early morning but

https://doi.org/10.5194/egusphere-2026-5208
Preprint. Discussion started: 28 September 2026

frequently reaches or exceeds the summit during daytime (Ok et al., 2026). The site therefore alternates among boundary-layer-decoupled, transitional, and boundary-layer-coupled conditions. This variability provides an opportunity to test whether enhanced PAN is preferentially associated with periods of local boundary-layer isolation or persists across changing vertical-coupling regimes.

Boundary-layer decoupling alone, however, does not identify the origin or processing history of PAN-rich air. PAN observed above a shallow nocturnal boundary layer may reflect continental transport, but reactive nitrogen and volatile organic compounds emitted within Korea can also undergo daytime photochemical processing and be transported vertically through mixed-layer growth, terrain-driven circulation, convection, or synoptic lifting. Processed air may subsequently remain within an elevated residual layer and undergo regional transport or recirculation. Conversely, PAN formed over continental East Asia can reach the Korean Peninsula within a vertically extensive pollution layer. Distinguishing these influences therefore requires consideration of both local boundary-layer coupling and the preceding air-mass pathway.

Interpretation of reactive-nitrogen reservoirs is further complicated by the non-selective response of heated molybdenum converters used in routine chemiluminescence NO_2 measurements. In addition to NO_2, these converters can reduce HNO_3, PAN and other peroxyacyl nitrates, and organic nitrates to NO, producing a positive interference in reported NO_2 concentrations (Dunlea et al., 2007; Jung et al., 2017). The difference between molybdenum-converter NO_2 and selectively measured photolytic-converter NO_2 can therefore provide an operational indicator of gas-phase oxidized nitrogen beyond NO_2. Here we denote this difference as operational gas-phase NO_z^* (= $NO_{2,Moly} - NO_{2,Photo}$). NO_z^* is distinct from total atmospheric NO_z (= $NO_y - NO_x$) and is not interpreted as a complete oxidized-nitrogen mass balance because converter response efficiencies, inlet transmission, and measurement coverage are species dependent. Instead, it provides an observational framework for evaluating the relative abundance of directly measured PAN within the converter-responsive oxidized-nitrogen signal.

In this study, we combine synchronized photolytic- and molybdenum-converter NO_2 measurements from the same spring periods in 2022 and 2023 with direct PAN observations in 2023, MARGA measurements of HONO and HNO_3 in 2022, ERA5 boundary-layer diagnostics, and 72 h HYSPLIT backward trajectories at Mount Gaya. We address three related questions: (1) how large and reproducible is the operational gas-phase NO_z^* signal at this elevated receptor, and what fraction of its campaign-mean magnitude is represented by directly measured PAN; (2) does PAN abundance or PAN/NO_z^* vary systematically with local boundary-layer coupling; and (3) how do PAN abundance and its relative contribution to operational NO_z^* differ among Continental East Asia, Korean Peninsula regional, and Marine/Background air-mass pathways? We additionally examine PAN-rich episodes to determine whether the largest PAN enhancements and the highest PAN/NO_z^* ratios occur under the same transport conditions. Together, these analyses test whether PAN persistence at an elevated East Asian receptor is governed primarily by local boundary-layer isolation or instead reflects the combined influence of continental transport, regional photochemical processing, and vertical exchange.

https://doi.org/10.5194/egusphere-2026-5208
Preprint. Discussion started: 28 September 2026

2 Measurements and Methods

2.1 Site description and campaign design

Measurements were conducted at the summit of Mount Gaya (36.70° N, 126.62° E; 678 m a.s.l.) in western Korea, approximately 45 km east of the Yellow Sea (Fig. 1). The site is a rural elevated receptor with limited influence from immediate local emission sources. Because the summit elevation is comparable to the daytime depth of the regional planetary boundary layer (PBL), the site can alternately sample air above and within the local boundary layer, while also being influenced by regionally transported air. Mount Gaya is therefore not treated here as a permanently isolated free-tropospheric site. Rather, its varying relationship to the PBL provides an opportunity to evaluate PAN under changing degrees of local vertical coupling and to distinguish these effects from those associated with the preceding air-mass transport pathway.

Observations from the same springtime period, 28 March–25 May, were analyzed for 2022 and 2023. NO, NO_2, and O_3 were measured continuously during both campaigns. Gas-phase HONO and HNO_3 measurements were available in 2022, whereas direct PAN measurements were conducted in 2023. Measurements used in the integrated analyses were averaged to 1 h resolution.

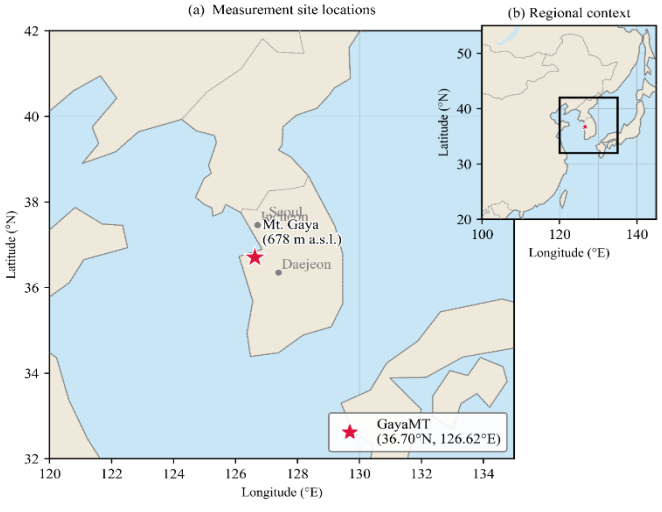

Figure 1: Location of the Mount Gaya summit measurement site (GayaMT; 678 m a.s.l.) and the regional context within East Asia. Coastlines are based on Natural Earth data (https://www.naturalearthdata.com).

2.2 PAN measurements and calibration

PAN was measured during the 2023 campaign at 10 min intervals using gas chromatography coupled with a pulsed-discharge electron-capture detector (GC-PDECD; Agilent 7890 GC equipped with a VICI D-2-220 detector). GC-based

https://doi.org/10.5194/egusphere-2026-5208
Preprint. Discussion started: 28 September 2026

electron-capture detection provides high sensitivity to peroxyacyl nitrates and has been widely applied to atmospheric PAN measurements. Ambient air was sampled through a 1/8-inch PEEK inlet installed approximately 10 m above the summit platform. PEEK tubing was used to minimize potential wall loss of PAN during sampling. PAN was chromatographically separated using a Restek RTX-200MS capillary column (15 m length, 0.53 mm inner diameter, 1 µm film thickness) maintained at 30 °C. PAN was identified from its retention time relative to a laboratory-generated PAN calibration mixture and from the reproducibility of the corresponding chromatographic peak.

The PAN calibration mixture was generated photochemically from NO and acetone under UV irradiation following established GC-based PAN generation approaches (Fischer et al., 2010; Flocke et al., 2005; Zhang et al., 2018). A 1 ppmv NO standard was introduced at 5 mL min^{-1} and mixed with a 20 ppmv acetone standard supplied at 40 mL min^{-1}. The effective irradiation volume was approximately 14.5 cm^3, corresponding to a precursor residence time of approximately 19.3 s at the combined precursor flow rate of 45 mL min^{-1}. The photochemically generated mixture was subsequently diluted with zero air to a total flow rate of approximately 1 L min^{-1}.

The nominal PAN mixing ratio generated upstream of the final dilution was calculated from the amount of NO supplied to the photochemical reactor, assuming a 1:1 molar relationship between converted NO and generated PAN:

$$C_{PAN,stock} = \eta_{PAN} C_{NO} \frac{Q_{NO}}{Q_{NO}+Q_{acetone}} \quad (1)$$

where C_{NO} is the mixing ratio of the NO standard, Q_{NO} and $Q_{acetone}$ are the corresponding precursor flow rates, and η_{PAN} is the apparent conversion factor relating consumed NO to generated PAN. For calculation of the nominal calibration concentration, quantitative conversion was assumed (η_{PAN} = 1). The experimental basis for this assumption and its limitations were evaluated independently as described below.

The performance of the photochemical generator was evaluated using a chemiluminescence NO_x analyzer equipped with a heated molybdenum converter. After UV irradiation, residual NO was below the instrumental detection limit of the chemiluminescence analyzer, while the oxidized-nitrogen response measured through the molybdenum-converter channel was approximately equivalent to the amount of NO introduced into the generator after accounting for dilution. These observations indicate near-complete consumption of the NO precursor and approximately quantitative recovery of the introduced nitrogen as molybdenum-converter-responsive oxidized nitrogen, suggesting that substantial loss of reactive nitrogen within the generator was unlikely.

Because the heated molybdenum converter is not chemically selective for PAN, however, this recovery experiment does not independently demonstrate that the chemical yield of PAN was exactly unity or that PAN constituted 100 % of the generated oxidized-nitrogen mixture. Accordingly, η_{PAN} = 1 was treated as a nominal calibration assumption, rather than as an independently verified PAN formation yield. This assumption was supported by the combined evidence of near-complete NO consumption, approximately quantitative recovery of the introduced nitrogen through the molybdenum-converter channel, the characteristic and reproducible GC-PDECD retention time of PAN, and the absence of additional major chromatographic peaks near the PAN retention time. The observed PAN response was also consistent with previous GC-

https://doi.org/10.5194/egusphere-2026-5208
Preprint. Discussion started: 28 September 2026

PDD/PDECD measurements using photochemically generated PAN standards (Zhang et al., 2018). Nevertheless, uncertainty in the actual PAN formation yield represents a potential systematic uncertainty in the absolute PAN calibration scale.

The generated PAN mixture was dynamically diluted with zero air to obtain multipoint calibration standards covering approximately 0.5–10 ppbv. Calibration curves were constructed by linear regression of integrated chromatographic peak area against the nominal PAN mixing ratio derived using Eq. (1). The instrumental detection limit for PAN was 0.01 ppbv, determined using the signal-to-noise criterion. PAN calibration was performed every two weeks throughout the campaign.

2.3 NO_x, HONO, and HNO_3 measurements and definition of operational NO_z^*

NO and NO_2 were measured using two chemiluminescence analyzers equipped with different NO_2-to-NO conversion techniques: a heated molybdenum converter (Mezus 210; Kentek, Republic of Korea) and a photolytic converter (Mezus 210P equipped with an AQD BLC2 converter; Kentek). The molybdenum converter was operated at approximately 320–325 ℃, whereas the photolytic converter used UV radiation centered near 395 nm and was maintained at approximately 45–50 °C. Both analyzers measured NO directly without converter activation. O_3 was measured by ultraviolet photometry (Mezus 410, Kentek, Korea).

The analyzers were calibrated using traceable NO-in-N_2 and NO_2-in-N_2 gas standards prepared by the Korea Research Institute of Standards and Science (KRISS). The molybdenum-converter efficiency for NO_2 was approximately 100 %, whereas the photolytic-converter efficiency was approximately 95 % at NO_2 mixing ratios below 100 ppbv. Photolytic NO_2 measurements were corrected for the experimentally determined conversion efficiency. The instrumental detection limits for individual NO and NO_2 measurements were approximately 0.4 ppbv. Calibration, linearity, instrumental drift, and converter-efficiency evaluations followed the procedures described by Jung et al. (2017).

The difference between the molybdenum-converter and photolytic-converter NO_2 measurements was defined as

$$NO_z^* = NO_{2,Moly} - NO_{2,Photo} \quad (2)$$

where NO_z^* is used as an operational indicator of gas-phase oxidized-nitrogen species contributing to the molybdenum-converter response beyond selectively measured NO_2. This operational definition is distinct from atmospheric NO_z, conventionally defined as

$$NO_z = NO_y - NO_x \quad (3)$$

Heated molybdenum converters can respond not only to NO_2 but also to PAN and other peroxyacyl nitrates, HNO_3, organic nitrates, and other oxidized-nitrogen compounds, with conversion efficiencies that vary among species. Photolytic-converter measurements are more selective for NO_2 but are not necessarily completely free of non-NO_2 responses, and species-dependent interferences have been reported for commercial photolytic systems (Villena et al., 2012; Reed et al., 2016). Previous field intercomparisons have consequently shown substantial differences between molybdenum-converter and more selective NO_2 measurements in rural, remote, and elevated environments influenced by aged and photochemically processed air (Steinbacher et al., 2007; Villena et al., 2012; Cowan et al., 2024).

https://doi.org/10.5194/egusphere-2026-5208
Preprint. Discussion started: 28 September 2026

The magnitude of the difference between the two systems depends on atmospheric composition as well as on species-dependent converter responses, inlet transmission, and potential non-NO_2 responses of the measurement systems. Accordingly, NO_z^* is not interpreted here as a quantitative measurement of total atmospheric NO_z or as a stoichiometrically closed oxidized-nitrogen budget. Rather, it represents an operational gas-phase difference signal that provides a common observational basis for evaluating the abundance of directly measured PAN relative to the converter-responsive oxidized-nitrogen signal. Both NO_2 measurement systems were equipped with upstream particulate-removal filters; particulate nitrate was therefore excluded from the converter-derived difference signal.

Gas-phase HONO and HNO_3 were measured during the 2022 campaign using a Measurement of Aerosols and Gases in Ambient Air system (MARGA 2060; Metrohm Process Analytics, the Netherlands). Ambient gas-phase species were collected using a wet rotating denuder and transferred to an aqueous absorption solution prior to ion-chromatographic analysis. HONO and HNO_3 were quantified from the corresponding nitrite and nitrate signals, respectively. Gas-phase samples were integrated over 1 h periods and analyzed semi-continuously by ion chromatography.

For analyses involving PAN/NO_z^*, the ratio was treated as an operational measurement ratio rather than as physical partitioning of a conserved reactive-nitrogen reservoir. Because NO_z^* is derived from the difference between two independently measured NO_2 signals and is subject to species-dependent converter responses and other measurement uncertainties, occasional hourly PAN/NO_z^* values exceeding unity can occur. Such observations were retained rather than truncated and were not interpreted as indicating that atmospheric PAN physically exceeded a closed NO_z inventory.

Observations with $NO_z^* \leq 0.4$ ppbv were excluded from the primary PAN/NO_z^* analysis to reduce numerical instability associated with small denominator values. The 0.4 ppbv criterion was applied as a pragmatic lower threshold and should not be interpreted as a formal detection limit or combined uncertainty of the NO_z^* difference signal. Sensitivity analyses were additionally performed using more restrictive thresholds of 0.8 and 1.0 ppbv. The frequency of hourly PAN/NO_z^* values exceeding unity was also evaluated across these thresholds to assess whether such excursions were preferentially associated with low operational NO_z^*.

2.4 Boundary-layer classification

Hourly planetary boundary-layer height (PBLH) and surface geopotential were obtained from the ERA5 single-level reanalysis through the Copernicus Climate Data Store (Hersbach et al., 2020). ERA5 fields were extracted for March–May 2023 from the grid point nearest to Mount Gaya (36.7029° N, 126.6221° E). The ERA5 horizontal grid spacing used for the extraction was approximately 0.25° (~28 km). All ERA5 timestamps were converted from UTC to Korea Standard Time (KST; UTC+9) before matching with the hourly chemical observations.

ERA5 PBLH is defined relative to the model surface and is therefore expressed as height above ground level (AGL). To compare the modeled boundary-layer top with the Mount Gaya summit elevation, ERA5 surface geopotential at the same grid point was converted to model-surface elevation above sea level using the standard gravitational acceleration (9.807 m s^{-2}). The PBL-top altitude above sea level was then calculated as

https://doi.org/10.5194/egusphere-2026-5208
Preprint. Discussion started: 28 September 2026

$$z_{PBL-top} = z_{surface} + PBLH \quad (4)$$

where $z_{surface}$ is the ERA5 model-surface elevation above sea level and PBLH is the ERA5 boundary-layer height above the model surface.

The resulting PBL-top altitude was compared with the actual Mount Gaya summit elevation of 678 m a.s.l. Because the ~0.25° ERA5 grid smooths the complex mountain terrain, the ERA5 model-surface elevation does not necessarily represent the actual summit elevation. The model-surface elevation was therefore used only to convert ERA5 PBLH from an AGL quantity to PBL-top altitude above sea level, whereas boundary-layer coupling was classified relative to the observed summit elevation.

To reduce sensitivity to uncertainties in reanalysis-derived PBLH and model topography over complex terrain, a ±100 m buffer was applied around the summit elevation. Conditions were classified as follows:

- Boundary-layer coupled: $\mathbf{z_{PBL-top}} \geq 778$ m a.s.l.
- Transitional: 578 m < $\mathbf{z_{PBL-top}}$ < 778 m a.s.l.
- Decoupled: $\mathbf{z_{PBL-top}} \leq 578$ m a.s.l.

The ±100 m buffer was introduced to avoid assigning observations for which the modeled PBL top lay close to summit level directly to either the coupled or decoupled category.

Differences in PAN and PAN/NO_z^* between boundary-layer-coupled and decoupled conditions were initially evaluated using the Mann–Whitney U test. Because successive hourly observations were temporally autocorrelated, day-block bootstrap confidence intervals were additionally calculated for coupled-minus-decoupled differences in median PAN and PAN/NO_z^*. Interpretation therefore emphasized bootstrap confidence intervals and median contrasts rather than significance tests based on hourly observations alone. The boundary-layer classification was also repeated using alternative buffer widths of 0, 50, 200, and 300 m around the Mount Gaya summit elevation to assess the sensitivity of the results to the specific classification threshold.

2.5 Backward-trajectory and air-mass pathway classification

Air-mass transport pathways were investigated using the Hybrid Single-Particle Lagrangian Integrated Trajectory model (HYSPLIT version 5.4.2; Stein et al., 2015) driven by NOAA Global Data Assimilation System (GDAS) 1° meteorological fields. Seventy-two-hour backward trajectories were initialized at Mount Gaya (36.70° N, 126.62° E) at 100 m above ground level (AGL) at 6 h intervals (00, 06, 12, and 18 UTC). Additional trajectories initialized at 500 and 1000 m AGL were calculated for diagnostic purposes, whereas the 100 m AGL trajectories were used for the pathway classification and statistical analyses reported here. Vertical motion was calculated using the GDAS omega field.

Trajectories were calculated from 27 March to 25 May 2023 to ensure complete temporal matching with chemical observations at the beginning of the measurement period. For each initialization time, all GDAS meteorological files intersecting the full 72 h backward interval were supplied to HYSPLIT. All scheduled trajectories were successfully

https://doi.org/10.5194/egusphere-2026-5208
Preprint. Discussion started: 28 September 2026

completed to −72 h. A total of 236 trajectory arrivals falling within the chemical-analysis period from 28 March to 25 May 2023 were retained for the pathway analysis.

Each 100 m AGL trajectory was assigned to one of three broad transport-pathway categories according to its 72 h endpoint and mean longitudinal position:

1. Continental East Asia: trajectories with 72 h endpoints within 95–128° E and 25–58° N and a mean pathway longitude west of 124° E.
2. Marine/Background: trajectories with 72 h endpoints east of 133° E, north of 54° N, or south of 20° N.
3. Korean Peninsula regional: trajectories not assigned to the two categories above and remaining primarily over the Korean Peninsula, Yellow Sea, and adjacent marine regions.

These categories were designed to distinguish broad preceding air-mass pathways and should not be interpreted as quantitative source attribution. Among the 236 trajectories used in the analysis, 71 (30.1 %) were classified as Continental East Asia, 127 (53.8 %) as Korean Peninsula regional, and 38 (16.1 %) as Marine/Background pathways.

For comparison with hourly chemical observations, each hourly measurement was assigned to the category of the temporally nearest 6 h trajectory arrival, provided that the time difference did not exceed 3 h. Because trajectories were available continuously at 6 h intervals throughout the analysis period, this procedure provided a unique pathway assignment without extending the temporal matching window beyond half of the trajectory-launch interval.

To reduce temporal pseudoreplication in pathway comparisons, statistical analyses were conducted primarily at the trajectory level. For each trajectory arrival, the median PAN mixing ratio and the median of hourly PAN/NO_z^* ratios satisfying NO_z^* > 0.4 ppbv within the ±3 h matching window were used as trajectory-level representative values. Overall differences among Continental East Asia, Korean Peninsula regional, and Marine/Background pathways were evaluated using the Kruskal–Wallis test. When the overall test was significant, pairwise comparisons were performed using Mann–Whitney U tests with Holm adjustment for multiple comparisons. Hourly pathway-assigned observations were retained for descriptive visualization, whereas statistical inference was based primarily on trajectory-level values.

PAN-rich episodes were defined as periods during which hourly PAN exceeded the campaign 90th-percentile concentration (1.25 ppbv) for at least 3 consecutive hours. For each episode, transport characteristics were evaluated using the number and category of 6 h trajectory arrivals within a broader transport window surrounding the concentration-defined core episode, rather than the number of hourly chemical observations assigned to each pathway. The broader transport windows were 5 April 18:00–7 April 12:00 KST for E1, 20 April 18:00–22 April 06:00 KST for E2, 9 May 18:00–11 May 06:00 KST for E3, and 22 May 18:00–24 May 06:00 KST for E4.

2.6 Statistical analysis and sensitivity evaluation

Associations among PAN, operational NO_z^*, photolytic NO_2, O_3, PBL-top altitude, and other measured variables were evaluated using Spearman rank correlation coefficients. Non-parametric statistical tests were used because several

https://doi.org/10.5194/egusphere-2026-5208
Preprint. Discussion started: 28 September 2026

atmospheric variables exhibited non-normal and skewed distributions. Statistical results were interpreted together with effect sizes, distributional overlap, and sensitivity analyses rather than from p values alone.

3 Results

3.1 Campaign characteristics and operational gas-phase NO_z^*

Paired photolytic- and molybdenum-converter NO_2 measurements revealed a persistent positive difference signal at Mount Gaya during both spring campaigns. Photolytic and molybdenum-converter NO_2 were positively correlated in 2022 and 2023 (Spearman $\rho = 0.74$ and 0.64, respectively; $p < 0.001$), but the molybdenum-converter measurements were systematically higher throughout both campaigns.

Mean photolytic NO_2 mixing ratios were 1.58 ± 1.53 ppbv in 2022 and 1.54 ± 1.24 ppbv in 2023, whereas molybdenum-converter NO_2 averaged 3.69 ± 1.87 and 3.65 ± 1.92 ppbv, respectively (Table 1). The resulting operational gas-phase NO_z^* (= NO_2,Moly − NO_2,Photo) averaged 2.12 ± 1.07 ppbv in 2022 and 2.12 ± 1.47 ppbv in 2023, with corresponding median values of 1.88 and 1.84 ppbv. Operational NO_z^* represented 57.5 % and 58.0 % of the mean molybdenum-converter response in 2022 and 2023, respectively. The temporal evolution of operational NO_z^* during the 2023 campaign is shown in Fig. 2b. The nearly identical campaign-mean NO_z^* values indicate that a substantial converter-derived non-NO_2 signal was reproducibly observed during the same springtime period in two consecutive years.

Table 1. Campaign summary statistics for the same springtime analysis period in 2022 and 2023. Values are mean ± standard deviation unless otherwise indicated. NO_z^* denotes the operational gas-phase difference NO_2,Moly − NO_2,Photo.

Parameter	2022	2023
O_3 (ppbv)	53.1 ± 15.6	52.5 ± 13.2
NO (ppbv)	0.55 ± 0.39	0.42 ± 0.37
NO_2,Photo (ppbv)	1.58 ± 1.53	1.54 ± 1.24
NO_2,Moly (ppbv)	3.69 ± 1.87	3.65 ± 1.92
NO_z^* (ppbv)	2.12 ± 1.07	2.12 ± 1.47
HONO (ppbv)	0.06 ± 0.03	–
HNO_3 (ppbv)	0.15 ± 0.08	–
PAN (ppbv)	–	0.64 ± 0.51
PAN/campaign-mean NO_z^* (%)	–	30.2

https://doi.org/10.5194/egusphere-2026-5208
Preprint. Discussion started: 28 September 2026

In 2022, simultaneous MARGA measurements showed mean HONO and HNO_3 mixing ratios of 0.055 and 0.145 ppbv, equivalent to 2.6 % and 6.8 % of campaign-mean NO_z^*, respectively. Together, these two measured inorganic gases were equivalent to 9.4 % of the mean operational NO_z^* signal. This cross-year comparison is used only as a first-order constraint on directly measured oxidized-nitrogen species because PAN was measured in 2023, whereas HONO and HNO_3 were available in 2022.

Direct PAN measurements in 2023 averaged 0.64 ± 0.51 ppbv, with a median of 0.56 ppbv (IQR: 0.29–0.85 ppbv) and a maximum of 4.29 ppbv (Fig. 2a). The ratio of campaign-mean PAN to campaign-mean NO_z^* was 30.2 %. PAN was more strongly correlated with operational NO_z^* ($\rho = 0.61$, $p < 0.001$) than with photolytic NO_2 ($\rho = 0.25$, $p < 0.001$) or O_3 ($\rho = 0.27$, $p < 0.001$), indicating that PAN covaried substantially with the converter-derived oxidized-nitrogen signal.

For hourly observations restricted to $NO_z^* > 0.4$ ppbv, the PAN/NO_z^* ratio had a mean of 32.6 % and a median of 29.9 % (IQR: 17.6–43.9 %) (Fig. 2c). Increasing the lower NO_z^* threshold to 0.8 and 1.0 ppbv resulted in median PAN/NO_z^* ratios of 29.1 % and 29.0 %, respectively. The limited change with increasing threshold indicates that the central tendency of the PAN/NO_z^* distribution was not driven primarily by unstable ratios at very low NO_z^*.

Among the 1311 hourly observations satisfying $NO_z^* > 0.4$ ppbv, 16 (1.2 %) had PAN/$NO_z^* > 1$. The frequency decreased to 0.59 % and 0.37 % when the NO_z^* threshold was increased to 0.8 and 1.0 ppbv, respectively. Twelve of the 16 values occurred at $NO_z^* \leq 1.0$ ppbv, and the median absolute excess of PAN over operational NO_z^* was only 0.14 ppbv. Thus, occasional ratios above unity were associated primarily with relatively small operational NO_z^* values and small absolute differences between PAN and NO_z^*, without materially affecting the campaign-scale median ratio.

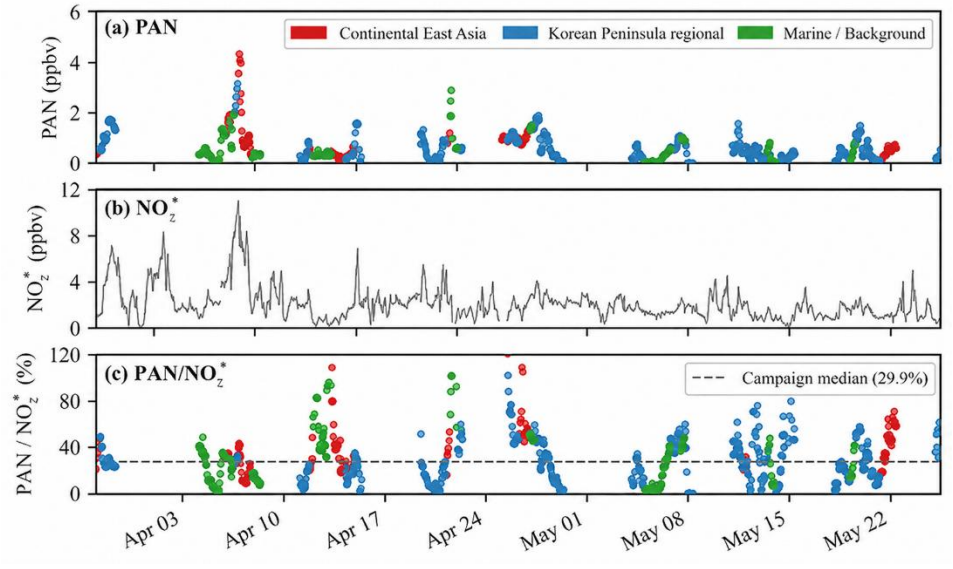

Figure 2. Campaign time series at Mount Gaya during spring 2023. (a) PAN mixing ratios colored by air-mass pathway category (Continental East Asia, Korean Peninsula regional, and Marine/Background). (b) Operational gas-

https://doi.org/10.5194/egusphere-2026-5208
Preprint. Discussion started: 28 September 2026

phase NO_z^* (= $NO_{2,Moly} - NO_{2,Photo}$). (c) Hourly PAN/$NO_z^*$ ratio for observations with NO_z^* > 0.4 ppbv. The dashed line indicates the campaign median hourly PAN/NO_z^* ratio of 29.9 %.

3.2 PAN variability across boundary-layer regimes

ERA5-derived PBL-top altitude varied substantially during the 2023 campaign, ranging from 61.5 to 1806 m a.s.l., with a mean of 485 ± 367 m a.s.l. and a median of 382 m a.s.l. Using the ±100 m classification buffer defined in Sect. 2.4, 65.8 % of observations were classified as decoupled, 21.9 % as boundary-layer coupled, and 12.3 % as transitional. Table 2 summarizes the corresponding PAN, operational NO_z^*, and PAN/NO_z^* statistics for the three boundary-layer regimes.

Table 2. PAN and operational NO_z^* statistics by ERA5-derived boundary-layer regime during spring 2023. PAN/NO_z^* statistics are restricted to observations with NO_z^* > 0.4 ppbv. Hours and percentages refer to observations with valid coincident PAN and PBL-regime assignments.

PBL regime	Hours (%)	PAN median (ppbv)	NO_z^* median (ppbv)	PAN/NO_z^* median (%)
Coupled	308 (21.9)	0.64	2.08	30.8
Transitional	172 (12.3)	0.59	1.93	30.3
Decoupled	924 (65.8)	0.54	1.82	29.7

PAN mixing ratios differed only modestly among the three boundary-layer regimes. Median PAN was highest under coupled conditions (0.64 ppbv), intermediate under transitional conditions (0.59 ppbv), and lowest under decoupled conditions (0.54 ppbv) (Table 2; Fig. 3c). Although a Mann–Whitney U test applied to the hourly observations indicated a significant coupled–decoupled difference ($p < 0.001$), the distributions overlapped substantially, and the day-block bootstrap estimate of the median difference was only 0.10 ppbv, with a 95 % confidence interval of −0.05 to 0.22 ppbv. Because this interval included zero, the apparent difference inferred from hourly observations was not robust after temporal autocorrelation was considered.

The relative abundance of PAN within operational NO_z^* showed even less dependence on boundary-layer regime. Median PAN/NO_z^* ratios were 30.8 % under coupled conditions, 30.3 % under transitional conditions, and 29.7 % under decoupled conditions (Table 2; Fig. 3d). The substantial overlap among the three distributions in Fig. 3d is consistent with the statistical analysis: the coupled–decoupled difference was not significant in the hourly Mann–Whitney comparison ($p = 0.14$), and the day-block bootstrap median difference was 1.2 percentage points with a 95 % confidence interval of −4.9 to 7.8 percentage points. PAN/NO_z^* therefore showed no systematic enhancement when Mount Gaya was decoupled from the local boundary layer.

The diurnal behavior provides additional context for these regime comparisons (Fig. 3a–b). Median PBL-top altitude increased markedly from approximately 200–300 m a.s.l. during nighttime to a maximum near 900 m a.s.l. during 13:00–15:00 KST, periodically rising above the summit elevation and increasing the likelihood of boundary-layer coupling (Fig.

https://doi.org/10.5194/egusphere-2026-5208
Preprint. Discussion started: 28 September 2026

3a). Median PAN also increased during the daytime, broadly coincident with the rise in PBL-top altitude, whereas the median PAN/NO_z^* ratio remained within a comparatively narrow range over the diurnal cycle (Fig. 3b). Thus, the diurnal changes were more apparent in absolute PAN abundance than in the relative magnitude of PAN within the operational NO_z^* signal.

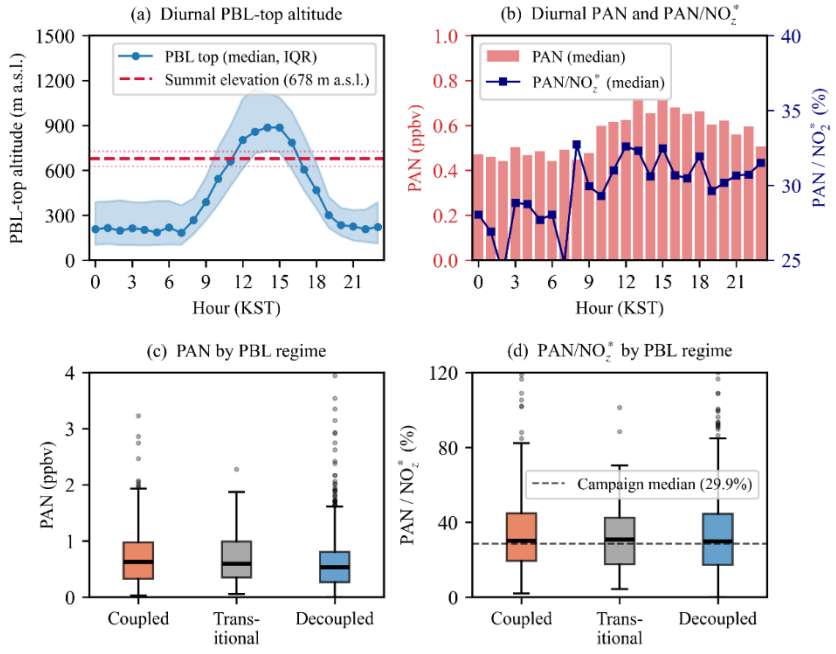

Figure 3. Influence of local boundary-layer coupling on PAN variability at Mount Gaya during spring 2023. (a) Diurnal variation in ERA5-derived PBL-top altitude; horizontal lines indicate the summit elevation (678 m a.s.l.) and the ±100 m classification bounds used to define coupled, transitional, and decoupled conditions. (b) Diurnal median PAN and PAN/NO_z^*. (c, d) Distributions of PAN and PAN/NO_z^* under boundary-layer-coupled, transitional, and decoupled conditions. The dashed line in (d) indicates the campaign median hourly PAN/NO_z^* ratio (29.9 %).

Taken together, Fig. 3 and Table 2 show that PAN concentrations tended to be somewhat higher during periods of boundary-layer coupling, but the magnitude of this contrast was small relative to the within-regime variability and was not robust after temporal autocorrelation was accounted for. The near-constant PAN/NO_z^* ratio across regimes provides even stronger evidence that boundary-layer coupling alone did not control the relative abundance of PAN at Mount Gaya.

Sensitivity tests using PBL classification buffers of 0, 50, 200, and 300 m produced the same qualitative result, with no consistent enhancement of PAN/NO_z^* under decoupled conditions. The principal interpretation was therefore insensitive to the exact PBL-height threshold used to define coupling. Together with the weak regime dependence shown in Fig. 3 and Table 2, these results indicate that local boundary-layer coupling alone could not explain the observed PAN variability, motivating the air-mass pathway analysis presented in Sect. 3.3.

https://doi.org/10.5194/egusphere-2026-5208
Preprint. Discussion started: 28 September 2026

3.3 PAN dependence on air-mass pathway

Backward-trajectory analysis revealed systematic differences in PAN abundance among the three air-mass pathway categories during the 2023 campaign. Of the 236 complete 72 h trajectories included in the analysis, 71 (30.1 %) were classified as Continental East Asia, 127 (53.8 %) as Korean Peninsula regional, and 38 (16.1 %) as Marine/Background pathways (Table 3). Thus, Korean Peninsula regional pathways represented the most frequently sampled transport regime, whereas approximately one-third of the trajectories reflected continental influence. These categories represent broad preceding transport histories rather than quantitative source contributions.

The spatial distributions of the trajectories further illustrate the contrast among these pathway categories (Fig. 4). Continental East Asia trajectories generally extended westward across northeastern China and the Yellow Sea before arriving at Mount Gaya, whereas Korean Peninsula regional trajectories remained more frequently over the peninsula, the Yellow Sea, and adjacent coastal regions. Marine/Background trajectories approached primarily from eastern or southern marine sectors. When the trajectories were colored by the PAN concentration associated with each arrival, many of the highest PAN values were associated with trajectories extending across continental East Asia and the Yellow Sea (Fig. 4a). Elevated PAN was nevertheless also observed along Korean Peninsula regional pathways, indicating that high PAN at Mount Gaya was not restricted to direct continental outflow.

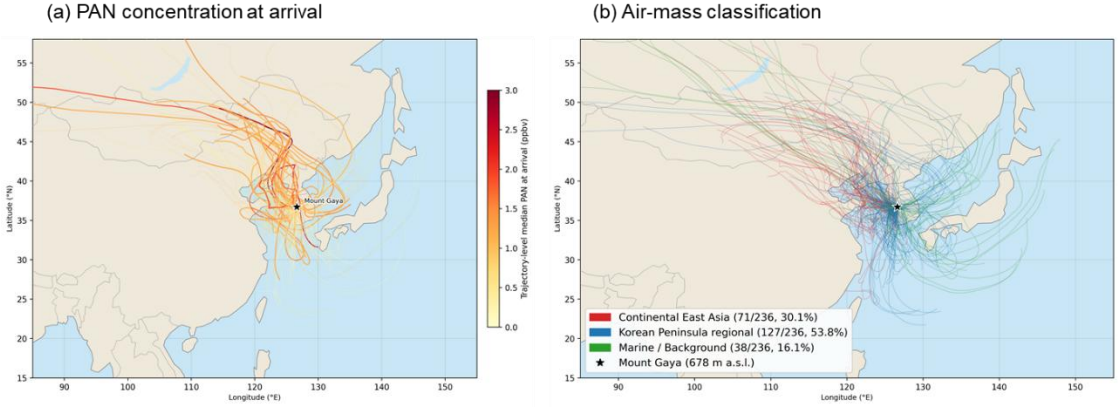

Figure 4. Seventy-two-hour HYSPLIT backward trajectories arriving at Mount Gaya (star) at 100 m AGL during spring 2023. (a) Trajectories colored by the representative PAN mixing ratio associated with each 6 h trajectory arrival. Values >3 ppbv are shown at the upper color limit. (b) Trajectories colored by air-mass pathway category. Bold trajectories indicate arrivals within the predefined PAN-rich episode transport windows.

To quantify these visual differences while reducing temporal pseudoreplication, statistical comparisons were based primarily on trajectory-level representative values obtained from the hourly chemical observations associated with each 6 h trajectory arrival. Table 3 summarizes the trajectory frequencies together with the corresponding PAN and PAN/NO_z^* distributions, while Fig. 5 shows the full trajectory-level distributions for the three pathway categories.

https://doi.org/10.5194/egusphere-2026-5208
Preprint. Discussion started: 28 September 2026

Table 3. PAN abundance and PAN/NO_z^* ratio by 72 h backward-trajectory pathway category during spring 2023. Trajectory fractions are based on the 236 complete trajectories included in the analysis. PAN and PAN/NO_z^* statistics are based on trajectory-level representative values derived from hourly observations associated with each trajectory arrival. PAN/NO_z^* calculations are restricted to observations with NO_z^* > 0.4 ppbv.

Pathway	Trajectories, n (%)	PAN median [IQR] (ppbv)	PAN/NO_z^* median [IQR] (%)
Continental East Asia	71 (30.1)	0.66 [0.43–0.85]	33.2 [22.0–44.8]
Korean Peninsula regional	127 (53.8)	0.58 [0.26–0.88]	28.2 [17.5–43.0]
Marine/Background	38 (16.1)	0.35 [0.27–0.64]	28.5 [11.0–42.6]

Median trajectory-level PAN differed significantly among the three pathway categories (Kruskal–Wallis H = 9.66, p = 0.008). Continental East Asia pathways showed the highest median PAN concentration, 0.66 ppbv (IQR: 0.43–0.85 ppbv), followed by Korean Peninsula regional pathways at 0.58 ppbv (IQR: 0.26–0.88 ppbv) and Marine/Background pathways at 0.35 ppbv (IQR: 0.27–0.64 ppbv) (Fig. 5a; Table 3). Pairwise comparisons indicated that the clearest contrast occurred between Continental East Asia and Marine/Background pathways (Mann–Whitney U test, Holm-adjusted p = 0.0058), whereas the other pairwise differences were not statistically significant after adjustment for multiple comparisons. The combination of the trajectory map and the trajectory-level distributions therefore indicates that continental transport was associated with the highest overall PAN abundance, while Korean Peninsula regional pathways maintained intermediate PAN levels.

PAN/NO_z^* showed a weaker dependence on pathway category. Median trajectory-level PAN/NO_z^* was 33.2 % (IQR: 22.0–44.8 %) for Continental East Asia pathways, 28.2 % (IQR: 17.5–43.0 %) for Korean Peninsula regional pathways, and 28.5 % (IQR: 11.0–42.6 %) for Marine/Background pathways (Fig. 5b; Table 3). Although the continental category had the highest median value, the distributions overlapped substantially and the overall difference among pathway categories was not statistically significant (Kruskal–Wallis H = 4.08, p = 0.130). Thus, transport history was more clearly associated with the absolute abundance of PAN than with the relative abundance of PAN within the operational NO_z^* signal.

https://doi.org/10.5194/egusphere-2026-5208
Preprint. Discussion started: 28 September 2026

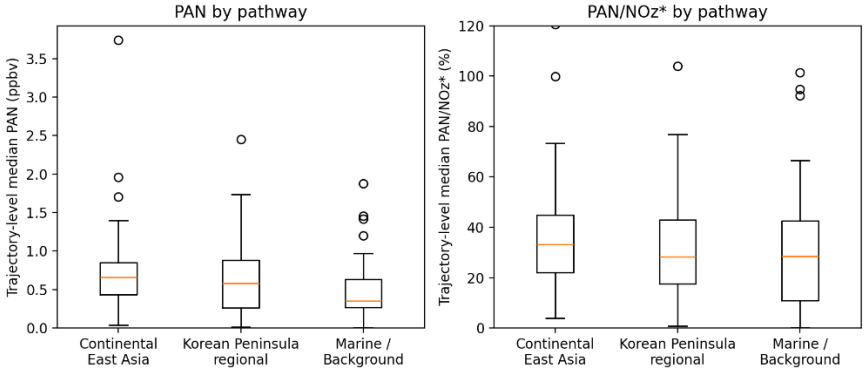

Figure 5. Trajectory-level PAN mixing ratio (a) and PAN/NO_z^* ratio (b) by air-mass pathway category. Representative chemical values were derived from hourly observations associated with each 6 h trajectory arrival. PAN/NO_z^* calculations are restricted to observations with NO_z^* > 0.4 ppbv. Boxes indicate the interquartile range and median, and whiskers extend to 1.5 × IQR.

The PAN-rich episodes provide additional context for the pathway dependence observed at the campaign scale. During the E1 transport window, 4 of 7 trajectories (57.1 %) were classified as Continental East Asia, whereas E2 was dominated by Korean Peninsula regional pathways (3 of 6 trajectories, 50.0 %), with only 1 of 6 trajectories (16.7 %) classified as Continental East Asia. All six trajectories during the E3 transport window were classified as Continental East Asia, while E4 showed a mixed pathway distribution, with 3 of 6 Continental East Asia, 2 of 6 Korean Peninsula regional, and 1 of 6 Marine/Background trajectories. These episode-to-episode contrasts indicate that elevated PAN can occur under different transport histories and that high PAN abundance and high PAN/NO_z^* ratios do not necessarily coincide with the same pathway conditions.

3.4 PAN-rich episodes

Four PAN-rich episodes were identified during the 2023 campaign using the criterion of at least 3 consecutive hours above the campaign 90th-percentile PAN concentration (1.25 ppbv): 6–7 April (E1), 21 April (E2), 10 May (E3), and 23 May (E4). Table 4 summarizes their PAN, operational NO_z^*, O_3, and pathway characteristics, while Fig. 6 shows the temporal evolution of PAN, NO_z^*, and PAN/NO_z^* during and around each core episode. Maximum PAN mixing ratios ranged from 2.86 to 4.29 ppbv, substantially above the campaign mean of 0.64 ppbv (Table 4).

Table 4. Summary of the four PAN-rich episodes and associated operational NO_z^*, O_3, and air-mass pathway characteristics during spring 2023. PAN, NO_z^*, PAN/NO_z^*, and O_3 statistics refer to the concentration-defined core episode periods. PAN/NO_z^* values are arithmetic means of hourly ratios. Pathway counts refer to 6 h trajectory arrivals within the predefined, broader episode transport windows. The broader transport windows used for

https://doi.org/10.5194/egusphere-2026-5208
Preprint. Discussion started: 28 September 2026

trajectory classification were 5 April 18:00–7 April 12:00 KST for E1, 20 April 18:00–22 April 06:00 KST for E2, 9 May 18:00–11 May 06:00 KST for E3, and 22 May 18:00–24 May 06:00 KST for E4.

Event	Core episode period	PAN mean (ppbv)	PAN max (ppbv)	NO_z^* mean (ppbv)	Mean hourly PAN/NO_z^* (%)	O_3 max (ppbv)	Pathway composition within transport window
E1	6 Apr 00:00–7 Apr 02:00	2.16	4.29	7.14	29.5	71.1	Continental 4/7; Korean regional 1/7; Marine/Background 2/7
E2	21 Apr 13:00–16:00	2.27	2.86	2.55	89.9	55.0	Continental 1/6; Korean regional 3/6; Marine/Background 2/6
E3	10 May 12:00–18:00	2.03	2.92	3.47	58.0	86.7	Continental 6/6
E4	23 May 11:00–18:00	2.00	3.23	3.32	59.7	79.4	Continental 3/6; Korean regional 2/6; Marine/Background 1/6

The strongest absolute PAN enhancement occurred during E1, when PAN averaged 2.16 ppbv and reached a maximum of 4.29 ppbv. Operational NO_z^* was also strongly elevated, with a mean of 7.14 ppbv, the highest among the four episodes (Table 4). The time series shows that PAN increased together with a broad enhancement in operational NO_z^*, while PAN/NO_z^* remained comparatively moderate, with a mean hourly ratio of 29.5 % (Fig. 6). Within the E1 transport window, 4 of 7 trajectories (57.1 %) were classified as Continental East Asia, compared with 1 Korean Peninsula regional and 2 Marine/Background trajectories. E1 therefore represents a case in which strong PAN enhancement coincided with a large increase in the broader converter-responsive oxidized-nitrogen signal under substantial, although not exclusive, continental influence.

E2 showed markedly different behavior. Mean PAN reached 2.27 ppbv, comparable to E1, but mean operational NO_z^* was much lower at 2.55 ppbv. Consequently, the arithmetic mean of the hourly PAN/NO_z^* ratios during the core episode reached 89.9 %, the highest among the four episodes (Table 4). This contrast is evident in Fig. 6, where PAN increased strongly without the large concurrent NO_z^* enhancement observed during E1, producing a pronounced increase in PAN/NO_z^*. The associated transport window was dominated by Korean Peninsula regional pathways, which accounted for 3 of 6 trajectories (50.0 %); only 1 of 6 trajectories (16.7 %) was classified as Continental East Asia, and 2 of 6 as Marine/Background. Thus, the episode with the highest operational PAN/NO_z^* ratio did not coincide with the strongest continental pathway influence.

https://doi.org/10.5194/egusphere-2026-5208
Preprint. Discussion started: 28 September 2026

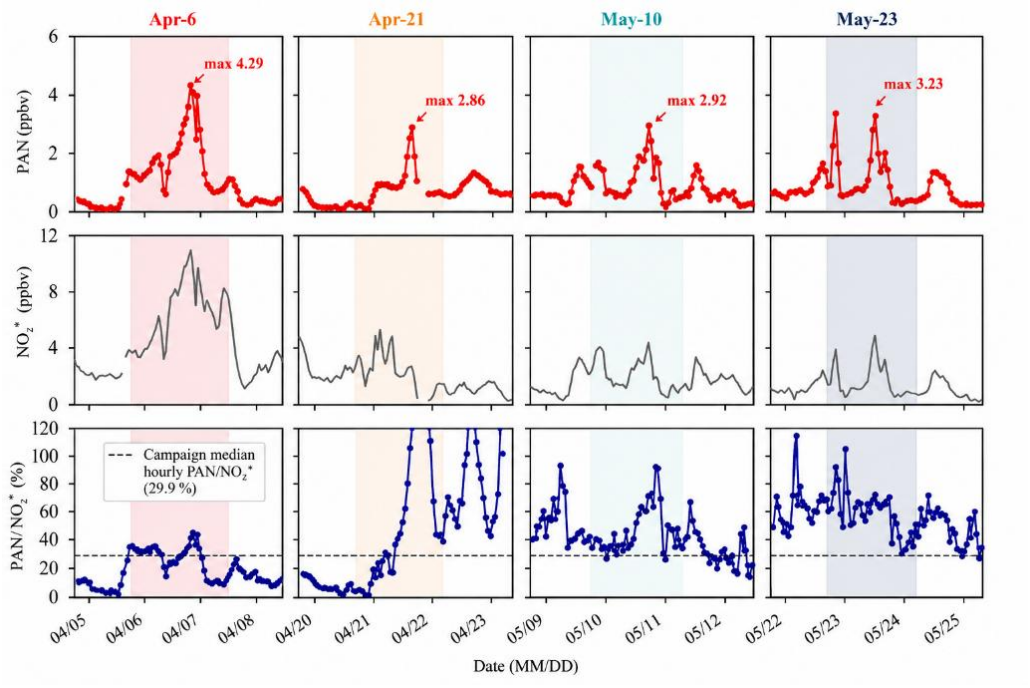

Figure 6. Time series of PAN, operational gas-phase NO_z^*, and PAN/NO_z^* during the four PAN-rich episodes. Shading indicates the concentration-defined core episode periods, and the time axis extends 24 h before and after each episode. PAN/NO_z^* values are shown only for observations satisfying the primary NO_z^* > 0.4 ppbv criterion. The dashed line indicates the campaign median hourly PAN/NO_z^* ratio of 29.9 %. Occasional values exceeding 100 % were retained because PAN/NO_z^* is treated as an operational measurement ratio rather than as physical partitioning of a closed reactive-nitrogen reservoir.

E3 had a mean PAN mixing ratio of 2.03 ppbv and a maximum of 2.92 ppbv, while mean operational NO_z^* was 3.47 ppbv and the mean hourly PAN/NO_z^* ratio was 58.0 % (Table 4; Fig. 6). All six trajectories within the E3 transport window were classified as Continental East Asia. E3 therefore provides a second clear example, in addition to E1, of elevated PAN associated with continental transport. However, its PAN/NO_z^* ratio was substantially higher than that of E1 but lower than that of E2, further illustrating that absolute PAN abundance and its relative magnitude within operational NO_z^* do not vary in parallel.

E4 showed a mean PAN mixing ratio of 2.00 ppbv and a maximum of 3.23 ppbv. Mean operational NO_z^* was 3.32 ppbv, with a mean hourly PAN/NO_z^* ratio of 59.7 % (Table 4). The temporal evolution in Fig. 6 shows a relatively sustained PAN/NO_z^* enhancement compared with E1, while the associated transport history was more heterogeneous. Of the six trajectories within the E4 transport window, three were classified as Continental East Asia, two as Korean Peninsula regional, and one as Marine/Background. Elevated PAN therefore also occurred under mixed transport conditions, without a single pathway category dominating the entire transport window.

https://doi.org/10.5194/egusphere-2026-5208
Preprint. Discussion started: 28 September 2026

O_3 maxima also varied among the episodes, from 55.0 ppbv during E2 to 86.7 ppbv during E3, with intermediate maxima of 71.1 and 79.4 ppbv during E1 and E4, respectively (Table 4). The episode with the highest PAN/NO_z^* ratio therefore did not coincide with the highest O_3 level, further emphasizing that PAN abundance, operational PAN/NO_z^*, and O_3 enhancement reflect related but not identical aspects of the evolving photochemical air mass.

Taken together, the four episodes illustrate distinct combinations of PAN abundance, operational NO_z^*, and transport history. Continental influence was substantial during E1 and exclusive within the E3 transport window, whereas E2 developed under predominantly Korean Peninsula regional pathways and exhibited the highest PAN/NO_z^* ratio. E4 occurred under mixed transport conditions. The contrasting temporal behavior shown in Fig. 6, together with the quantitative summary in Table 4, indicates that continental transport can strongly enhance PAN abundance, whereas a high operational PAN/NO_z^* ratio does not require dominant continental influence and may also reflect regional photochemical processing and changes in the broader oxidized-nitrogen mixture.

4 Discussion

4.1 PAN as a directly quantified component of operational gas-phase NO_z^*

The Mount Gaya observations revealed a persistent operational gas-phase oxidized-nitrogen signal during two consecutive spring campaigns. Operational NO_z^* represented approximately three-fifths of the molybdenum-converter NO_2 response in both 2022 and 2023, with an identical campaign-mean value of 2.12 ppbv. Such a large converter difference is consistent with previous comparisons at rural and elevated sites, where molybdenum-converter NO_2 measurements were strongly influenced by oxidized-nitrogen species in aged and photochemically processed air (Steinbacher et al., 2007). The reproducibility of the Mount Gaya difference signal across the same spring period in two consecutive years indicates that a similar converter-derived difference was consistently observed during both campaigns.

Direct PAN measurements in 2023 showed that the ratio of campaign-mean PAN to campaign-mean NO_z^* was 30.2 %, consistent with the median hourly PAN/NO_z^* ratio of 29.9 %. Increasing the lower NO_z^* threshold from 0.4 to 0.8 and 1.0 ppbv changed the median ratio only slightly, to 29.1 % and 29.0 %, respectively. The central tendency of PAN/NO_z^** was therefore insensitive to the treatment of small denominator values. Occasional hourly ratios exceeding unity occurred, but these represented a small fraction of the observations and were concentrated mainly at relatively low NO_z^*. As discussed in Sect. 2.3, such excursions are not interpreted as physical partitioning of a closed reactive-nitrogen reservoir because NO_z^* is an operational difference between two independent NO_2 measurements and is affected by species-dependent converter responses and measurement uncertainties.

Recent field studies reinforce the need for this operational interpretation. Molybdenum converters do not necessarily respond quantitatively or uniformly to individual NO_z species, and their effective response depends on atmospheric composition. For example, Cowan et al. (2024) inferred an apparent conversion of only about one-third of independently measured atmospheric NO_z compounds by a molybdenum-converter analyzer at a low-NO_x rural site. Together with earlier instrument

https://doi.org/10.5194/egusphere-2026-5208
Preprint. Discussion started: 28 September 2026

intercomparisons (Steinbacher et al., 2007; Villena et al., 2012), this finding demonstrates that the molybdenum–photolytic difference should not be interpreted as a stoichiometric measure of atmospheric NO_z. Accordingly, the PAN/NO_z^* values reported here are used to characterize PAN relative to the converter-responsive oxidized-nitrogen signal rather than to quantify its true fraction of total atmospheric reactive nitrogen.

The 2022 MARGA measurements provide a first-order comparison with two inorganic oxidized-nitrogen species. Mean HONO and HNO_3 were equivalent to 2.6 % and 6.8 % of campaign-mean NO_z^*, respectively, or 9.4 % combined. Because PAN and the MARGA species were measured in different years, this comparison does not constitute a simultaneous chemical budget, nor can the corresponding percentages be interpreted as directly additive fractions of atmospheric NO_z. Nevertheless, the nearly identical campaign-mean NO_z^* values in 2022 and 2023 provide useful context for comparing the characteristic magnitude of the directly measured oxidized-nitrogen species during the same spring season.

The portion of operational NO_z^* not associated with the directly measured species should therefore not be interpreted as a missing atmospheric NO_z fraction. Potential contributors include other peroxyacyl nitrates, organic nitrates, and gas-phase HNO_3, while differences in inlet transmission and species-dependent responses of both converter systems may also affect the measured difference signal. Resolving this remaining signal will require simultaneous speciated NO_y measurements together with characterization of converter responses to individual oxidized-nitrogen compounds.

Within these limitations, the 2023 PAN observations demonstrate that PAN represented a substantial directly measured component of the operational converter-responsive signal. Its persistent presence at Mount Gaya, together with its strong covariance with operational NO_z^*, supports an important role for PAN as a reservoir and carrier of reactive nitrogen capable of redistributing NO_x-derived ozone-production potential away from source regions.

4.2 Boundary-layer coupling and the elevated regional pollution layer

The absence of a robust contrast between boundary-layer-coupled and decoupled conditions indicates that local PBL position alone did not determine PAN-rich conditions at Mount Gaya. PAN abundance differed only modestly among coupling regimes, and PAN/NO_z^* showed no systematic enhancement when the summit was decoupled from the local boundary layer after temporal autocorrelation was considered.

This result cautions against interpreting enhanced PAN at an elevated receptor solely as evidence of isolated free-tropospheric air. Mount Gaya frequently transitions among decoupled, transitional, and coupled conditions, so the sampled air can reflect varying combinations of residual-layer influence, regional transport, and daytime boundary-layer exchange. PAN persistence across these regimes is therefore more consistent with sampling a vertically extensive regional pollution layer than with a simple separation between boundary-layer and free-tropospheric reservoirs.

The diurnal behavior provides additional context for this interpretation. PBL-top altitude increased markedly during daytime, and PAN mixing ratios also tended to increase. However, the present observations cannot separate the respective contributions of daytime photochemistry, vertical exchange, and changing air-mass history. PAN/NO_z^* remained

https://doi.org/10.5194/egusphere-2026-5208
Preprint. Discussion started: 28 September 2026

comparatively stable over the diurnal cycle, indicating that the diurnal variation was more pronounced in absolute PAN abundance than in its relative magnitude within the converter-responsive oxidized-nitrogen signal.

Taken together, the boundary-layer analysis indicates that PBL height is useful for diagnosing the local vertical relationship between the summit and the underlying atmosphere but does not identify the origin or processing history of PAN-rich air. The air-mass pathway analysis therefore provides an essential complementary constraint.

4.3 Continental outflow and Korean Peninsula regional pathways

Air-mass pathway analysis showed that PAN abundance at Mount Gaya reflected both continental transport and regional atmospheric processing. Continental East Asia pathways exhibited the highest trajectory-level PAN concentrations, and the overall pathway dependence of PAN was statistically significant, with the clearest contrast between Continental East Asia and Marine/Background pathways. This pattern is consistent with the transport of PAN-rich air from upwind East Asian source regions and with preservation of PAN during regional transport. Previous modeling and observational studies have likewise shown that PAN can redistribute reactive nitrogen from East Asian source regions and influence downwind ozone chemistry over regional to trans-Pacific scales (Jiang et al., 2016; Zhai et al., 2024).

Elevated PAN, however, was not confined to continental pathways. Korean Peninsula regional pathways were the most frequently sampled category and showed intermediate PAN concentrations between Continental East Asia and Marine/Background conditions. This is consistent with recent observations of widespread acyl peroxynitrate enhancements over South Korea and the adjacent Yellow Sea (Lee et al., 2026), suggesting that PAN-rich air can persist within the regional atmosphere even when trajectories do not indicate dominant continental outflow. Regional photochemical production, transport of PAN precursors, vertical redistribution, and repeated circulation within the Korean Peninsula–Yellow Sea region may all contribute to maintaining PAN at Mount Gaya.

In contrast to absolute PAN abundance, PAN/NO_z^* showed only a weak dependence on pathway category. Although the median trajectory-level PAN/NO_z^* ratio was highest for Continental East Asia pathways, the overall difference among the three pathway categories was not statistically significant. This indicates that transport history exerted a clearer influence on the amount of PAN reaching Mount Gaya than on the relative abundance of PAN within the broader converter-responsive oxidized-nitrogen signal. The latter likely depends not only on PAN but also on variations in other oxidized-nitrogen species and on species-dependent responses of the two NO_2 measurement systems.

The four PAN-rich episodes further illustrate this distinction. E1 occurred under substantial Continental East Asia influence and exhibited both the highest absolute PAN concentration and the largest operational NO_z^* enhancement. E3 provides an additional continental case, with all six trajectories in its transport window classified as Continental East Asia, but its PAN/NO_z^* ratio was substantially lower than that of E2. In contrast, E2 was dominated by Korean Peninsula regional pathways and exhibited the highest PAN/NO_z^* ratio despite limited continental influence. E4 occurred under mixed continental, regional, and marine pathways while still showing substantial PAN enhancement. These cases demonstrate that

https://doi.org/10.5194/egusphere-2026-5208
Preprint. Discussion started: 28 September 2026

continental transport can strongly enhance absolute PAN abundance, whereas a high PAN/NO_z^* ratio does not uniquely diagnose continental influence.

The observations therefore point to two non-exclusive processes. Continental transport can deliver PAN-rich air from upwind East Asian source regions, while regional photochemical processing and redistribution can maintain substantial PAN within the lower-tropospheric pollution layer over and around the Korean Peninsula. Because the trajectory categories describe broad preceding air-mass histories rather than quantitative source contributions, these contrasts should not be interpreted as source apportionment.

The coexistence of continental and regional influences supports the interpretation of Mount Gaya as an elevated receptor that can sample a vertically extensive regional pollution layer under differing transport and boundary-layer conditions. PAN observed at the summit therefore reflects interactions among long-range transport, regional chemistry, and vertical exchange rather than a single continental or free-tropospheric source regime.

4.4 Atmospheric implications and limitations

PAN provides an efficient mechanism for redistributing reactive nitrogen and ozone-production potential away from emission regions. Through reversible thermal decomposition, PAN can retain NO_x-derived reactive nitrogen during transport and release NO_2 when transported air warms or mixes downward. The Mount Gaya observations indicate that this reservoir persists within an elevated East Asian pollution layer influenced by both continental outflow and regional atmospheric processing. The occurrence of substantial PAN under both boundary-layer-coupled and decoupled conditions further suggests that reactive nitrogen stored as PAN can remain available within the regional lower troposphere across changing vertical-coupling regimes.

The substantial PAN abundance relative to operational NO_z^* also has implications for the interpretation of routine NO_2 measurements. Heated molybdenum converters respond to PAN and other oxidized-nitrogen compounds in addition to NO_2, and previous field intercomparisons have demonstrated substantial converter interference in aged, rural, and elevated air masses (Steinbacher et al., 2007; Villena et al., 2012; Cowan et al., 2024). The persistent molybdenum–photolytic difference observed at Mount Gaya is consistent with these findings and demonstrates that non-NO_2 oxidized-nitrogen compounds can make a substantial contribution to the apparent NO_2 response in photochemically processed air. Selective NO_2 measurements combined with direct measurements of individual reactive-nitrogen species are therefore important for interpreting both NO_2 concentrations and the regional transport of oxidized nitrogen.

Several limitations constrain the quantitative interpretation of the present observations. First, PAN was measured directly only in 2023, whereas HONO and HNO_3 were available in 2022. Although campaign-mean operational NO_z^* was nearly identical during the same spring period in the two years, the comparison among these species represents a first-order cross-year context rather than a simultaneous oxidized-nitrogen budget. Second, NO_z^* is an operational difference between two independently measured NO_2 signals rather than a direct measurement of atmospheric NO_z. Species-dependent molybdenum-converter efficiencies, possible non-NO_2 responses of the photolytic system, and differential inlet transmission

https://doi.org/10.5194/egusphere-2026-5208
Preprint. Discussion started: 28 September 2026

can all affect the magnitude of this difference. In particular, transmission of relatively low-volatility or surface-reactive species such as HNO_3 was not independently characterized for the two sampling systems. PAN/NO_z^* should therefore be interpreted as an operational measurement ratio rather than as the physical partitioning of a conserved reactive-nitrogen reservoir. Occasional hourly ratios exceeding unity further illustrate this distinction and are not interpreted as evidence that PAN physically exceeded a closed atmospheric NO_z inventory.

The transport analysis also has inherent limitations. The HYSPLIT categories represent broad preceding air-mass pathways rather than quantitative source contributions, and deterministic trajectories driven by 1° GDAS meteorological fields are subject to uncertainty in both horizontal position and vertical transport. Although complete 72 h trajectory coverage was obtained for the analysis period, individual trajectory positions remain sensitive to meteorological resolution and uncertainties in modeled vertical motion. Consequently, the pathway contrasts identify differences in transport history but do not separate the contributions of continental emissions, regional photochemical production, recirculation, and vertical redistribution. Ensemble trajectories, higher-resolution meteorological fields, vertical profiling, and chemical transport modeling would provide additional constraints on these processes.

Despite these limitations, the combined observations consistently show that PAN is a substantial directly measured component of the converter-responsive oxidized-nitrogen signal at Mount Gaya and that its persistence cannot be explained by local boundary-layer isolation alone. Instead, the boundary-layer and trajectory analyses together point to the combined influence of continental transport, regional photochemical processing, and vertical exchange. These findings highlight PAN as an important pathway for redistributing reactive nitrogen within and downwind of East Asia and emphasize the need to account for both atmospheric transport history and measurement selectivity when evaluating regional oxidized-nitrogen and ozone chemistry.

5 Conclusions

This study examined PAN at Mount Gaya, an elevated receptor in East Asia, using paired photolytic- and molybdenum-converter NO_2 measurements, direct PAN observations, ERA5 boundary-layer diagnostics, and HYSPLIT backward trajectories. A persistent operational gas-phase NO_z^* signal was observed during two consecutive spring campaigns, with identical campaign-mean values of 2.12 ppbv in 2022 and 2023, corresponding to approximately 58 % of the molybdenum-converter NO_2 response. In 2023, PAN averaged 0.64 ± 0.51 ppbv, and the ratio of campaign-mean PAN to campaign-mean NO_z^* was 30.2 %. This ratio represents an operational relative measure rather than a complete atmospheric NO_z budget.

PAN persistence was not explained by local boundary-layer isolation alone. Differences in PAN abundance between boundary-layer-coupled and decoupled conditions were not robust after temporal autocorrelation was considered, and PAN/NO_z^* showed no systematic dependence on boundary-layer regime. In contrast, PAN abundance varied significantly among air-mass pathways, with Continental East Asia pathways showing the highest trajectory-level PAN concentrations and the clearest contrast relative to Marine/Background pathways. PAN/NO_z^*, however, showed a weaker and statistically non-significant dependence on pathway category. PAN-rich episodes further demonstrated that the largest absolute PAN

https://doi.org/10.5194/egusphere-2026-5208
Preprint. Discussion started: 28 September 2026

enhancement and the highest PAN/NO_z^* ratio occurred under different transport conditions. Together, these results support an elevated regional pollution-layer framework in which continental transport, regional photochemical processing, and vertical exchange jointly influence PAN persistence at Mount Gaya.

The results demonstrate that PAN can represent a substantial directly measured component of converter-responsive oxidized nitrogen at an elevated East Asian receptor. They also show that transport history exerted a clearer influence on absolute PAN abundance than either local boundary-layer coupling or the relative PAN/NO_z^* ratio. Combining selective NO_2 measurements with direct PAN observations, boundary-layer diagnostics, and air-mass trajectory analysis therefore provides a useful framework for investigating reactive-nitrogen redistribution in East Asia. Future work incorporating simultaneous speciated NO_y measurements, vertical profiling, ensemble trajectories, and chemical transport modeling will be needed to resolve the remaining operational NO_z^* signal and quantify the consequences of PAN-mediated reactive-nitrogen transport for regional ozone chemistry.

These findings are consistent with previous observational and modeling studies showing that PAN can transport reactive nitrogen from East Asian source regions and remain abundant over the Korean Peninsula and adjacent seas (Jiang et al., 2016; Zhai et al., 2024; Lee et al., 2026), while extending those studies by explicitly separating local boundary-layer coupling from preceding transport history at a continuously monitored elevated receptor. The interpretation remains limited by the operational nature of NO_z^*, the absence of simultaneous speciated NO_y measurements, and uncertainties inherent in deterministic backward trajectories.

Code and data availability

The Mount Gaya PAN and related trace-gas measurement data used in this study are available at Zenodo at https://doi.org/10.5281/zenodo.21376215 (Jung, 2026).

Author contributions

J. Jung and S. Ok conducted the field campaign and wrote the manuscript. J. Y. Lee reviewed and revised the manuscript.

Competing interests

The authors declare that they have no conflict of interest.

Acknowledgements

The authors gratefully acknowledge the NOAA Air Resources Laboratory (ARL) for providing the HYSPLIT transport and dispersion model used in this study.

https://doi.org/10.5194/egusphere-2026-5208
Preprint. Discussion started: 28 September 2026

Financial support

This work was supported by the Korea Research Institute of Standards and Science (KRISS) under the Basic R&D Project [Grant No. 26011043].

References

Cowan, N., Twigg, M. M., Leeson, S. R., Jones, M. R., Harvey, D., Simmons, I., Coyle, M., Kentisbeer, J., Walker, H., and Braban, C. F.: Assessing the bias of molybdenum catalytic conversion in the measurement of NO_2 in rural air quality networks, Atmos. Environ., 322, 120375, https://doi.org/10.1016/j.atmosenv.2024.120375, 2024.

Dunlea, E. J., Herndon, S. C., Nelson, D. D., Volkamer, R. M., San Martini, F., Sheehy, P. M., Zahniser, M. S., Shorter, J. H., Wormhoudt, J. C., Lamb, B. K., Allwine, E. J., Gaffney, J. S., Marley, N. A., Grutter, M., Marquez, C., Blanco, S., Cardenas, B., Retama, A., Ramos Villegas, C. R., Kolb, C. E., Molina, L. T., and Molina, M. J.: Evaluation of nitrogen dioxide chemiluminescence monitors in a polluted urban environment, Atmos. Chem. Phys., 7, 2691–2704, https://doi.org/10.5194/acp-7-2691-2007, 2007.

Fischer, E. V., Jaffe, D. A., Reidmiller, D. R., and Jaeglé, L.: Meteorological controls on observed peroxyacetyl nitrate at Mount Bachelor during the spring of 2008, J. Geophys. Res.-Atmos., 115, D03302, https://doi.org/10.1029/2009JD012776, 2010.

Fischer, E. V., Jaffe, D. A., and Weatherhead, E. C.: Free tropospheric peroxyacetyl nitrate (PAN) and ozone at Mount Bachelor: Potential causes of variability and timescale for trend detection, Atmos. Chem. Phys., 11, 5641–5654, https://doi.org/10.5194/acp-11-5641-2011, 2011.

Fischer, E. V., Jacob, D. J., Yantosca, R. M., Sulprizio, M. P., Millet, D. B., Mao, J., Paulot, F., Singh, H. B., Roiger, A., Ries, L., Talbot, R. W., Dzepina, K., and Pandey Deolal, S.: Atmospheric peroxyacetyl nitrate (PAN): A global budget and source attribution, Atmos. Chem. Phys., 14, 2679–2698, https://doi.org/10.5194/acp-14-2679-2014, 2014.

Flocke, F. M., Weinheimer, A. J., Swanson, A. L., Roberts, J. M., Schmitt, R., and Shertz, S.: On the measurement of PANs by gas chromatography and electron capture detection, J. Atmos. Chem., 52, 19–43, https://doi.org/10.1007/s10874-005-6772-0, 2005.

Flowerday, C. E. and Hansen, J. C.: Peroxyacetyl nitrate (PAN) in the atmosphere: A comprehensive review of chemistry, measurements, and chemical-transport implications, Environ. Sci.: Atmos., https://doi.org/10.1039/D6EA00017G, 2026.

Hersbach, H., Bell, B., Berrisford, P., Hirahara, S., Horányi, A., Muñoz-Sabater, J., Nicolas, J., Peubey, C., Radu, R., Schepers, D., Simmons, A., Soci, C., Abdalla, S., Abellan, X., Balsamo, G., Bechtold, P., Biavati, G., Bidlot, J., Bonavita, M., De Chiara, G., Dahlgren, P., Dee, D., Diamantakis, M., Dragani, R., Flemming, J., Forbes, R., Fuentes, M., Geer, A., Haimberger, L., Healy, S., Hogan, R. J., Hólm, E., Janisková, M., Keeley, S., Laloyaux, P., Lopez, P., Lupu, C., Radnoti, G., de Rosnay, P., Rozum, I., Vamborg, F., Villaume, S., and Thépaut, J.-N.: The ERA5 global reanalysis, Q. J. Roy. Meteor. Soc., 146, 1999–2049, https://doi.org/10.1002/qj.3803, 2020.

https://doi.org/10.5194/egusphere-2026-5208
Preprint. Discussion started: 28 September 2026

Hu, B., Chen, N., Li, R., Huang, M., Chen, J., Hong, Y., Xu, L., Fan, X., Li, M., Tong, L., Zheng, Q., and Yang, Y.: Understanding summertime peroxyacetyl nitrate (PAN) formation and its relation to aerosol pollution: Insights from high-resolution measurements and modeling, Atmos. Chem. Phys., 25, 905–921, https://doi.org/10.5194/acp-25-905-2025, 2025.

Jiang, Z., Worden, J. R., Payne, V. H., Zhu, L., Fischer, E. V., Walker, T. W., and Jones, D. B. A.: Ozone export from East Asia: The role of PAN, J. Geophys. Res.-Atmos., 121, 6555–6563, https://doi.org/10.1002/2016JD024952, 2016.

Jung, J., Lee, J. Y., Kim, B. M., and Oh, S. H.: Seasonal variations in the NO_2 artifact from chemiluminescence measurements with a molybdenum converter at a suburban site in Korea (downwind of the Asian continental outflow) during 2015–2016, Atmos. Environ., 165, 290–300, https://doi.org/10.1016/j.atmosenv.2017.07.010, 2017.

Jung, J.: PAN 2022–2023_MT Gaya data, Zenodo [data set], https://doi.org/10.5281/zenodo.21376215, 2026.

Laughner, J. L., Kulawik, S. S., and Payne, V. H.: An algorithm to retrieve peroxyacetyl nitrate from AIRS, Atmos. Meas. Tech., 19, 249–276, https://doi.org/10.5194/amt-19-249-2026, 2026.

Lee, Y. R., Arterburn, L., Takeuchi, M., Tanner, D. J., Roberts, J. M., Roozitalab, B., Jeong, D., Hills, A. J., Hornbrook, R. S., Apel, E. C., Meinardi, S., Barletta, B., Blake, N. J., Blake, D. R., Kim, S., Wojnowski, W., Piel, F., Wisthaler, A., Ball, K., Crounse, J. D., Wennberg, P. O., Miech, J., Choi, Y., DiGangi, J. P., Diskin, G. S., Sebol, A., Delaria, E. R., Hannun, R. A., St. Clair, J. M., Wolfe, G. M., Cho, C., Owen, C., Lesko, K., Franchin, A., Winstead, E. L., Ziemba, L. D., Moore, R., Wiggins, E. B., Symonds, G., Kim, D., Day, D. A., Campuzano-Jost, P., Jimenez, J. L., Ullmann, K., Hall, S. R., Crawford, J. H., and Huey, L. G.: Wintertime photochemistry of acyl peroxynitrates and ozone in South Korea during the ASIA-AQ campaign, Atmos. Chem. Phys., 26, 8695–8715, https://doi.org/10.5194/acp-26-8695-2026, 2026.

Lin, Z., Xu, L., Yang, C., Chen, G., Ji, X., Li, L., Zhang, K., Hong, Y., Li, M., Fan, X., Hu, B., Zhang, F., and Chen, J.: Trends of peroxyacetyl nitrate and its impact on ozone over 2018–2022 in urban atmosphere, npj Clim. Atmos. Sci., 7, 192, https://doi.org/10.1038/s41612-024-00746-7, 2024.

Liu, T., Wang, Y., Cai, H., Wang, H., Zhang, C., Chen, J., Dai, Y., Zhao, W., Li, J., Gong, D., Chen, D., Zhai, Y., Zhou, Y., Liao, T., and Wang, B.: Complexities of peroxyacetyl nitrate photochemistry and its control strategies in contrasting environments in the Pearl River Delta region, npj Clim. Atmos. Sci., 7, 116, https://doi.org/10.1038/s41612-024-00669-3, 2024.

Ok, S., Lee, J. Y., and Jung, J.: Vertical contrasts in $PM_{2.5}$ composition and diagnostic evaluation of surface nitrate enhancement in western Korea, Atmos. Environ., 382, 122191, https://doi.org/10.1016/j.atmosenv.2026.122191, 2026.

Reed, C., Evans, M. J., Di Carlo, P., Lee, J. D., and Carpenter, L. J.: Interferences in photolytic NO_2 measurements: Explanation for an apparent missing oxidant?, Atmos. Chem. Phys., 16, 4707–4724, https://doi.org/10.5194/acp-16-4707-2016, 2016.

Shogrin, M. J., Payne, V. H., Kulawik, S. S., Miyazaki, K., and Fischer, E. V.: Changes to peroxyacyl nitrates (PANs) over megacities in response to COVID-19 tropospheric NO_2 reductions observed by the Cross-Track Infrared Sounder (CrIS), Geophys. Res. Lett., 51, e2023GL104854, https://doi.org/10.1029/2023GL104854, 2024.

https://doi.org/10.5194/egusphere-2026-5208
Preprint. Discussion started: 28 September 2026

Shogrin, M. J., Payne, V. H., Kulawik, S. S., Miyazaki, K., and Fischer, E. V.: Transport of peroxyacyl nitrates (PANs) across Northern Hemisphere ocean basins from satellite observations, J. Geophys. Res.-Atmos., 131, e2025JD044872, https://doi.org/10.1029/2025JD044872, 2026.

Stein, A. F., Draxler, R. R., Rolph, G. D., Stunder, B. J. B., Cohen, M. D., and Ngan, F.: NOAA's HYSPLIT atmospheric transport and dispersion modeling system, Bull. Am. Meteorol. Soc., 96, 2059–2077, https://doi.org/10.1175/BAMS-D-14-00110.1, 2015.

Steinbacher, M., Zellweger, C., Schwarzenbach, B., Bugmann, S., Buchmann, B., Ordóñez, C., Prévôt, A. S. H., and Hueglin, C.: Nitrogen oxide measurements at rural sites in Switzerland: Bias of conventional measurement techniques, J. Geophys. Res.-Atmos., 112, D11307, https://doi.org/10.1029/2006JD007971, 2007.

Villena, G., Bejan, I., Kurtenbach, R., Wiesen, P., and Kleffmann, J.: Interferences of commercial NO_2 instruments in the urban atmosphere and in a smog chamber, Atmos. Meas. Tech., 5, 149–159, https://doi.org/10.5194/amt-5-149-2012, 2012.

Zhai, S., Jacob, D. J., Franco, B., Clarisse, L., Coheur, P.-F., Shah, V., Bates, K. H., Lin, H., Dang, R., Sulprizio, M. P., Huey, L. G., Moore, F. L., Jaffe, D. A., and Liao, H.: Transpacific transport of Asian peroxyacetyl nitrate (PAN) observed from satellite: Implications for ozone, Environ. Sci. Technol., 58, 9760–9769, https://doi.org/10.1021/acs.est.4c01980, 2024.

Zhang, L., Jaffe, D. A., Gao, X., and McClure, C. D.: A quantification method for peroxyacetyl nitrate (PAN) using gas chromatography (GC) with a non-radioactive pulsed discharge detector (PDD), Atmos. Environ., 179, 23–30, https://doi.org/10.1016/j.atmosenv.2018.02.008, 2018.